Materials & Design 259 (2025) 114723

Contents lists available at ScienceDirect

Materials & Design

journal homepage: www.elsevier.com/locate/matdes

DNN-based shape optimization of gradient-index phononic crystals with sensitivity analysis for tunable focal position and robust energy harvesting

Mary Kim [a,b], Sangryun Lee [a,b,*]

[a] Graduate Program in System Health Science and Engineering, Ewha Womans University, Seoul 03760, Republic of Korea
[b] Department of Mechanical and Biomedical Engineering, Ewha Womans University, Seoul 03760, Republic of Korea

ARTICLE INFO

Keywords:
Phononic crystal
Energy harvesting
Genetic algorithm
Deep neural network
Sensitivity analysis

ABSTRACT

Gradient-index (GRIN) phononic crystals (PnCs) enable energy harvesting (EH) by focusing elastic waves into electrical energy. Efficient EH requires maximizing focused wave intensity, typically achieved by tuning the GRIN PnCs unit-cell shape. However, existing designs often exhibit energy concentration near the GRIN lens boundary and incorporate narrow gaps and sharp corners, making them susceptible to manufacturing errors and limiting their practical applicability. Understanding the potential performance changes caused by manufacturing errors is important because geometrical alterations can compromise wave-focusing performance. Therefore, this study aims to optimize the unit-cell shape toward maximum focused intensity at the desired locations for EH devices. To assess manufacturability, the effects of minor geometric variations on the focal position and focused intensity are evaluated via a sensitivity analysis. The optimal shape is derived using a deep neural network (DNN) surrogate model trained to predict focal position and focused intensity. This model accelerates a genetic algorithm (GA) used to perform the optimization. Our optimized designs exhibit 1.5 to 2.0 times higher focused intensity across the target focal positions compared with the conventional design. Thus, these optimal shapes, along with their sensitivity analysis results, provide practical guidelines for defining manufacturing tolerances and achieving consistent, efficient EH performance.

1. Introduction

The growing global energy demand has accelerated efforts toward sustainable energy solutions. EH provides a viable approach to utilizing ambient energy from everyday environments [1–6]. Among EH technologies, piezoelectric EH converts mechanical energy into electrical energy, providing the small amounts of power required to operate sensors in various applications, such as biomedical devices [7,8], civil engineering [9–11], and smart systems [12–14]. With regard to artificially engineered structures for EH, phononic crystals (PnCs)—metamaterials with periodic structures designed to exhibit unconventional properties—have attracted attention [15–17]. PnCs form bandgaps for flexural elastic waves with wavelengths comparable to the length of the unit lattice constant, thereby prohibiting the propagation of elastic waves within a particular frequency range [18–22]. These unique properties have prompted the widespread use of PnCs in insulation [23–25], waveguiding [26–31], wave localization [32–34], and wave focusing [35–37].

Gradient-index (GRIN) PnCs facilitate wave focusing through spatial variations in their refractive index [38,39]. Recent GRIN PnC studies have explored various applications. Tol *et al.* [40] proposed a Luneburg GRIN lens capable of omnidirectional wave focusing, Shen *et al.* [41] superimposed defect modes onto GRIN PnCs to improve focusing performance, and Danawe *et al.* [42] integrated defect modes with GRIN PnCs for further enhancement. However, most GRIN PnC designs are based on circular or elliptical inclusions [43,44]. This preference is primarily because analytical modeling becomes challenging for complex shapes, as closed-form solutions are typically limited to simple geometries. This inherent difficulty has restricted the exploration of shape as a systematic design variable. Although numerical methods can handle complex inclusions, they are often computationally expensive, particularly in iterative design, where repeated evaluations of wave-scattering performance are required [45,46]. Therefore, recent research has employed DNNs, optimizing multi-dimensional input variables and achieving rapid inference [47–50]. Lee *et al.* [47] proposed a novel geometry for GRIN PnCs, which offers improved focusing performance compared to conventional designs. However, the strong energy concentration near lens boundaries limits practical harvester placement.

* Corresponding author.
E-mail address: sr.lee@ewha.ac.kr (S. Lee).

https://doi.org/10.1016/j.matdes.2025.114723
Received 25 June 2025; Received in revised form 17 August 2025; Accepted 8 September 2025
Available online 14 September 2025
0264-1275/© 2025 The Author(s). Published by Elsevier Ltd. This is an open access article under the CC BY-NC-ND license (http://creativecommons.org/licenses/by-nc-nd/4.0/).

And unlike the disorder-robust band gaps of plate–rod systems [51], the fabrication-driven discrepancies observed between GRIN PnCs experiments and simulations call for tolerance-aware, shape-robust unit-cell designs.

This study introduces an optimal unit-cell design for GRIN PnCs that enhances the focused intensity through a controlled focal position in view of practical EH requirements. The proposed approach explores how varying the focal position affects the intensity of the focused energy. This analysis provides a Pareto front that guides design decisions. High-order closed Bézier curves are used to represent unit-cell geometries, enabling flexible shape parametrization. An initial dataset of 30,000 random shapes is generated and evaluated using finite element analysis (FEA). The active learning process iterates until the shape converges with a high focused intensity at the target focal position. Additionally, the trained DNNs are employed to identify the design variables that significantly impact the output predictions. The optimized shapes undergo a sensitivity analysis to gain a comprehensive understanding of the relationship between the design variables and the performance outcomes. This finding helps explain the discrepancies between the simulation and experimental data from the previous study [47]. Ultimately, This study demonstrates enhanced wave focusing and robust EH in GRIN PnCs with a tunable focal position, enabling more efficient EH.

2. Methodology

2.1. Data generation

Piecewise Bézier curves are used to design flexible and closed unit-cell shapes. Specifically, 12 independent cubic Bézier curves are stitched together to form a closed curve within a unit cell measuring 5 mm × 5 mm (Figs. 1(a) and (b)). A Bézier curve is a parametric curve defined by the position of its control points, which enables the creation of smooth and flexible curves. The general form of a Bézier curve $\boldsymbol{B}(t)$ is expressed as follows:

$$\boldsymbol{B}(t) = \sum_{i=0}^{n} \binom{n}{i} \boldsymbol{P}_i (1-t)^{n-i} t^i, \quad t \in [0,1] \tag{1}$$

where $\boldsymbol{P}_i$ is the i-th control point, and n is the order of the Bézier curve. In this study, 12 cubic Bézier curves are generated every 30°, providing uniform angular coverage with an appropriate number of design variables. This configuration covers the practical focal position range while balancing geometric flexibility, manufacturability, and simulation efficiency. To ensure smooth connections at the boundary points where the curves meet, C^0, C^1, and C^2 continuity conditions are satisfied at the start and end points of each curve. Each Bézier curve comprises four control points, the coordinates of two of which are automatically determined by the continuity conditions. Consequently, the closed curves are defined by 12 independent control points. These closed Bézier curves are designed to avoid self-intersection and have a minimum curvature radius exceeding 0.1 mm to ensure manufacturability. These curves are then scaled and translated such that the generated shape is positioned 0.5 mm away from the unit-cell boundaries for structure stability.

The GRIN lens is constructed by arranging the closed Bézier curves periodically. The size ratio of the shapes along the perpendicular direction of the GRIN lens follows the values in Table 1, as suggested in the previous study [47]. The GRIN lens has an overall size of 65 mm × 80 mm and comprises a 13 × 8 array of unit cells (Fig. 1(c)). To reduce the FEA computation time, a half-size model of the full GRIN plate is used, with the symmetry condition applied to the yz plane (Fig. S1). Time-harmonic simulations are conducted in COMSOL Multiphysics 6.1

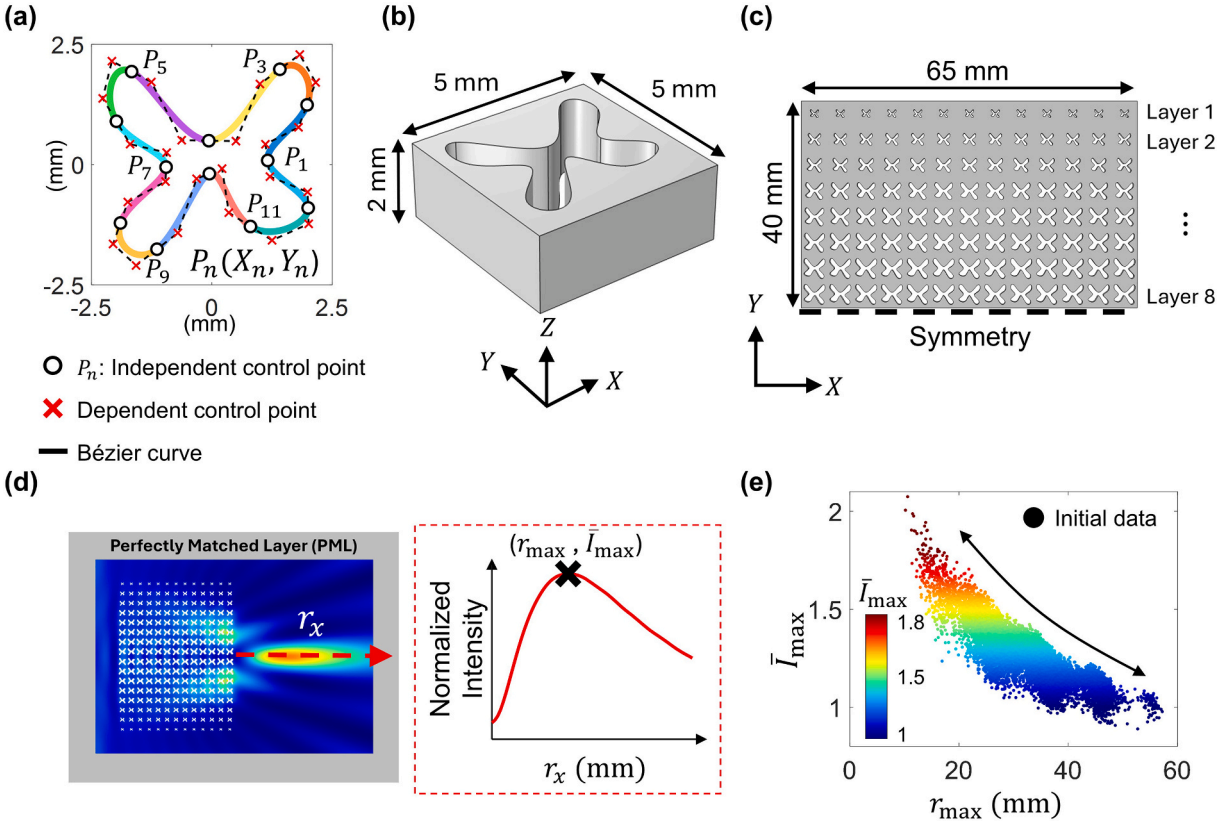


Fig. 1. Initial dataset preparation. (a) Definition of unit-cell shape using 12 Bézier curve segments. (b) Dimensions of unit cell and GRIN lens. (c) GRIN lens comprising a 13 × 8 arrangement of unit cells, with a scale factor applied to the unit-cell shape in the y direction for each layer. (d) FEA results of GRIN PnCs showing the focused intensity normalized to that of the circular shape, with $(r_{max}, \bar{I}_{max})$ determined from the 1D symmetry line. (e) Scatter plots illustrating $(r_{max}, \bar{I}_{max})$ against initial dataset, with smaller r_{max} values corresponding to higher $\bar{I}_{max}$ values.

Table 1
Size ratio of shapes for each layer of GRIN lens.

Layer number	Scale factor
Layer 1	0.4
Layer 2	0.6
Layer 3	0.7
Layer 4	0.85
Layer 5	0.9
Layer 6	0.95
Layer 7	1
Layer 8	1

using the Solid Mechanics module with Frequency Domain Study to predict the focal positions and focused intensities for GRIN lenses with random shapes [52]. The base material of the GRIN PnC plate is aluminum with the following material properties: density 2631.4 kg/m3, Young's modulus 70 GPa, and Poisson's ratio 0.33. A 1 N/m^2 traction with a 50 kHz frequency is induced in the z direction on the xz plane at one end of a 2-mm-thick GRIN plate, and a continuous incident shear wave is generated within the domain. To prevent any reflection of the generated flexural wave from the ends of the plate, an infinite plate is assumed by applying perfectly matched layers (PMLs) with a thickness of 15 mm to the outer domains of the GRIN plate (Fig. S1). The intensity (I) of the elastic wave is calculated as $I = \int |\boldsymbol{w}|^2 dt$, where $\boldsymbol{w}$ and t denote the transverse displacement and time, respectively. Based on the FEA results, the focused intensity lies along the symmetry line of the plate (Fig. 1(d)). The maximum intensity is determined along the 1D symmetry line of the plate, extending from the point where the GRIN lens ended to the PML boundary. The normalized focused intensity ($\bar{I}_{max}$) is obtained by normalizing the maximum intensity with respect to the focused intensity of the circular shapes. The corresponding focal position (r_{max}) of $\bar{I}_{max}$ is then identified. The FEA is performed for 30,000 random Bézier shapes, with the results showing that the elastic wave is focused at various positions. Fig. 1(e) shows the (r_{max}, $\bar{I}_{max}$) values predicted for the 30,000 shapes, highlighting the trade-off relationship between r_{max} and $\bar{I}_{max}$, i.e., the nearer the focal position is to the lens boundary, the higher is the focused intensity. An optimal unit-cell design is created to achieve $\bar{I}_{max}$ at r_{max} values of 15 mm, 20 mm, 25 mm, and 30 mm, ensuring a sufficient distance from the GRIN lens boundary to allow space for the piezoelectric EH device. Additionally, $\bar{I}_{max}$ is further optimized for focal positions at 10 mm, 40 mm, and 50 mm to derive a Pareto curve for the correlation between the focal position and the focused intensity.

2.2. Mesh convergence test

The focal position and focused intensity are evaluated for various element sizes to balance the computational efficiency and accuracy of the FEA. Fig. S2(a) shows that for the half-plate model, the mesh size decreases as the number of elements increases, with finer meshes concentrated along the boundaries of the inhomogeneous regions. Fig. S2(b) and (c) illustrate the dependence of the FEA results on the mesh size. Based on the mesh convergence results, the plate is generated with approximately 220,000 linear tetrahedral elements. To prevent stress concentration near the hole, the maximum mesh size is set to 2 mm, equivalent to 1/10 of the wavelength (λ) of the incident wave. Additionally, a finer mesh size of approximately $\lambda/20$ is applied along the centerline to predict the focused intensity accurately (Fig. S3). Compared with the smallest element size that can be computed with the maximum power of our hardware (Intel® Core™ i9-13900 K CPU@3.00 GHz), the aforementioned setting yields a 163 times faster computation, with sufficiently low relative errors of 9.3 % in focal position and 2.2 % in focused intensity.

Fig. S4 shows the FEA-derived focal positions and focused intensities for the initial 30,000 shapes. Due to the domain being discretized by a mesh, the smoothness of the intensity plot is insufficient for accurately predicting the focused intensity. Hence, the FEA results are interpolated to obtain a smooth and continuous intensity plot. Spline data are obtained at 0.1 mm intervals along the symmetry line, and the maximum intensity is re-estimated. This approach enables the prediction of $\bar{I}_{max}$ over a more continuous range of focal positions compared with the initial FEA data, providing a finer resolution at intermediate points that are previously unavailable in the discretized data. The interpolated results are compared with the reference value computed using the smallest element size to verify the interpolation accuracy. The raw data–based predictions with 200,000 elements exhibit a 4.9 % error in focal position and a 2.6 % error in focused intensity relative to the values predicted based on the reference results. In contrast, the spline data exhibit a 3.7 % error in focal position and a 2.6 % error in focused intensity, which underscores the improved accuracy achieved through the spline interpolation.

2.3. Optimization process

In this study, a unit-cell shape is designed using a DNN and a GA to maximize wave focusing at the target focal position (r_{target}). Conventional GRIN lens design typically involves tailoring a single unit cell to achieve a target local wave velocity and arranging these cells according to an analytical profile such as a hyperbolic sine distribution [43]. While computationally efficient, this approach assumes isotropic behavior and weak inter-cell coupling, which may not hold for complex or anisotropic geometries. In this study, the unit-cell shape is defined by high-order closed Bézier curves, producing anisotropic scattering and boundary effects that require full-structure optimization to accurately capture global wave propagation. This strategy enables simultaneous control of focal position and intensity while incorporating manufacturing constraints and sensitivity analysis to ensure robust performance. Moreover, the proposed data-driven optimization framework complements physical understanding by efficiently exploring design–performance relations that are analytically intractable, making it especially effective for complex metamaterial systems. Fig. 2 illustrates the overall workflow. The DNN is trained to understand the complicated relationship between the unit-cell shape, focal position (r_{max}), and normalized focused intensity ($\bar{I}_{max}$). Two fully connected DNNs, the architectures of which are shown in Fig. S5, are trained to predict r_{max} and I_{max} using the 12 control points of the closed Bézier curve as input, which are represented by 24 design variables comprising (x,y) coordinates. Each DNN comprises an input layer, an output layer, and 11 hidden layers, with each hidden layer containing 24 neurons. Batch normalization and a ResNet structure are employed, with skip connections used to prevent gradient vanishing [53]. A leaky ReLU function with a slope of 0.1 is used as the activation function. To verify the prediction accuracy, the 30,000 initial datasets are divided into training and test data in a 9:1 ratio. The mini-batch size is set to 500, and the DNN is trained for 150 epochs using the ADAM optimizer to minimize the root-mean-square error (RMSE) loss function. The learning rate is initially set to 0.01 and is multiplied by 0.01 every 50 epochs to ensure convergence during training. The loss and RMSE of the test data are assessed every 60 iterations to validate the network structure and hyperparameters. The hyperparameters used in this study are based on those from a previous study that optimized the focused intensity [47]. Since the focal position is also governed by linear elastic wave behavior, the same hyperparameters are adopted here. This configuration enables accurate predictions with a short training time (~126s) and fast inference speed (~3×10^{-5}s per shape) on our hardware.

The objective function (F) for the optimization is expressed as follows:

$$F(r_{max}, \bar{I}_{max}) = k\left|r_{max} - r_{target}\right| + \bar{I}_{max} \tag{2}$$

where r_{max} represents the predicted focal position, r_{target} denotes the

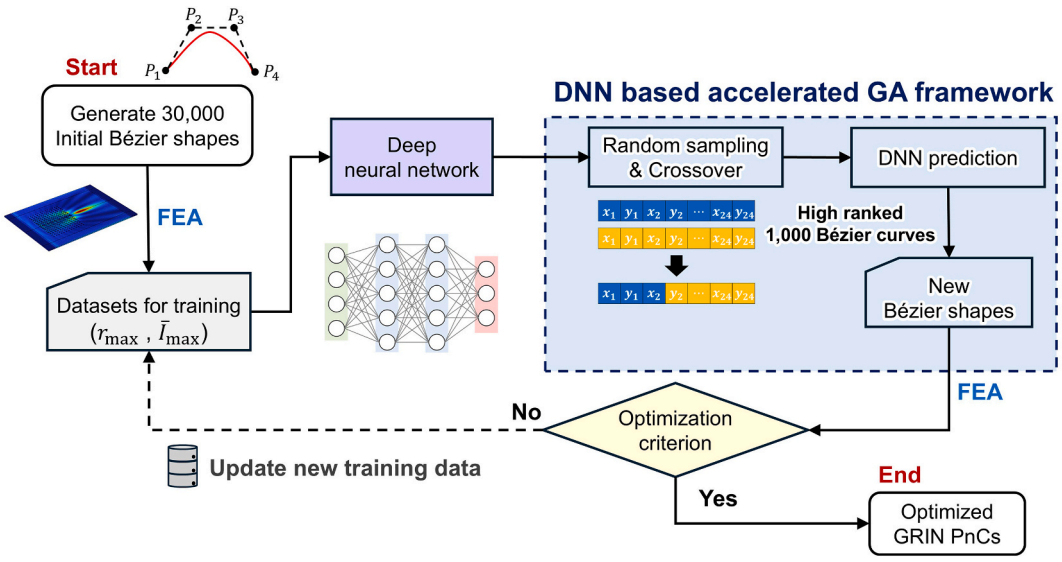


Fig. 2. Workflow diagram of DNN-based GA approach. The process begins with the generation of 30,000 random Bézier shapes, which are evaluated via FEA to predict r_{max} and $\bar{I}_{max}$ for DNN training. Two DNNs are employed to model the relationships between r_{max} and $\bar{I}_{max}$ for each shape. The GA utilizes random sampling to introduce mutation effects and crossover operations and thus generate offspring data. The trained DNNs serve as a surrogate model in the GA to rapidly generate offspring data with high objective function values. The offspring datasets are added to the existing datasets, and the process iterates until the optimization criterion is satisfied.

designated position for energy focusing, and k is the penalty coefficient. The penalty term acts as a constraint on r_{max} to ensure energy focusing at the target focal position by maximizing the objective function with a negative penalty coefficient. This approach ensures that r_{max} converges to r_{target} and that $\bar{I}_{max}$ reaches its maximum value. The optimization in this study is based on maximizing the $\bar{I}_{max}$ at the r_{max}. This choice is supported by previous GRIN PnC energy harvesting studies, where designs optimized for maximum focusing intensity achieved significant increases in harvested power without relying on a precise hyperbolic sine refractive index profile [47]. Since the electrical output of piezoelectric energy harvester scales with the square of the strain or velocity amplitude, maximizing $\bar{I}_{max}$ provides a reliable surrogate metric for improving EH performance. To achieve maximum intensity within the focal position range, k is set to −1 by trial and error, following a method proposed in a previous study [54].

An accelerated GA is then implemented with the aid of the NNs, which enable rapid inference. For the GA, each chromosome represents either the x-coordinate or y-coordinate of the control point, resulting in 24 design variables that define the hole shape. The initial dataset contains 30,000 random samples, providing a sufficiently broad design space for effective optimization. To promote diversity and prevent premature convergence, mutation is implemented by introducing 3,000 random samples in each generation. These samples are generated independently of existing chromosomes and enable exploration of previously unvisited regions of the design space. For crossover, a pair of parent chromosomes is selected from all possible combinations according to a probability distribution proportional to their objective function values. A single-point crossover is applied by randomly choosing a division point within the 24-dimensional design input. The offspring inherits the first segment from Parent 1, and the remaining segment from Parent 2. The resulting parameter set serves as a new design candidate for the Bézier curve design. The new Bézier curves are predicted by two trained DNNs for r_{max} and $\bar{I}_{max}$, and a candidate is adopted as new data if its objective function ranks within the top 0.3 % of all data. Leveraging DNNs for rapid inference significantly enhances computational efficiency [47,54]. Specifically, while the FEA-based predictions require 1–2 min per data sample, the DNNs provide predictions within a few seconds. The DNNs are updated by adding the newly acquired datasets to the existing dataset, which improves the prediction accuracy of the DNNs. Through active learning, the DNNs are trained on new data, and their weights are updated to enhance their prediction accuracy. The GA iterates over the entire dataset, which includes the data from the previous generation, until $\bar{I}_{max}$ converges while satisfying r_{target} through optimization.

3. Results and discussions

3.1. Leveraging DNN

As the training of the two DNNs progresses, the RMSEs for the training and test datasets both converge to below 10 % of the corresponding initial RMSEs. Figs. 3(a) and (b) show the results of DNN training in terms of the r_{max} and $\bar{I}_{max}$ values of the GRIN PnCs for the initial 30,000 datasets. To validate the performance of the DNNs in predicting the output variables from the input control points, the FEA results are used as the ground truth. The accuracy of the DNN predictions with respect to the FEA results is determined by fitting the dataset results to a $y = x$ curve (Figs. 3(c) and (d)). The NN models are observed to be successfully trained, showing a high R^2 exceeding 97 %. The R^2 of the models is also evaluated on the test dataset, and it exceeds 96 % for both r_{max} and $\bar{I}_{max}$, which confirms the high prediction accuracy of the DNNs.

Fig. 3(e) compares the objective function rankings predicted by the DNNs and the corresponding FEA results. Since the parent sets are selected based on their ranking of the objective function, the optimization performance depends on the accuracy of the ranking. Our trained DNNs accurately predict the rankings of r_{max} and $\bar{I}_{max}$ with respect to the ground-truth rankings. Fig. 3(f) illustrates the data distribution of the initial datasets and the datasets of the final generation for the target focal position. As the number of generations increases, the objective function output progressively increases, and new data are generated near the optimal point. Finally, r_{max} converges to r_{target}, and $\bar{I}_{max}$ reaches its maximum value. Fig. 3(g) highlights the improvement achieved in the focused intensity at the target position as the optimization progresses. The maximum value for the final generation indicates an improvement in performance compared with the maximum value for the initial dataset.

The impact of each design variable on the predictions by the trained

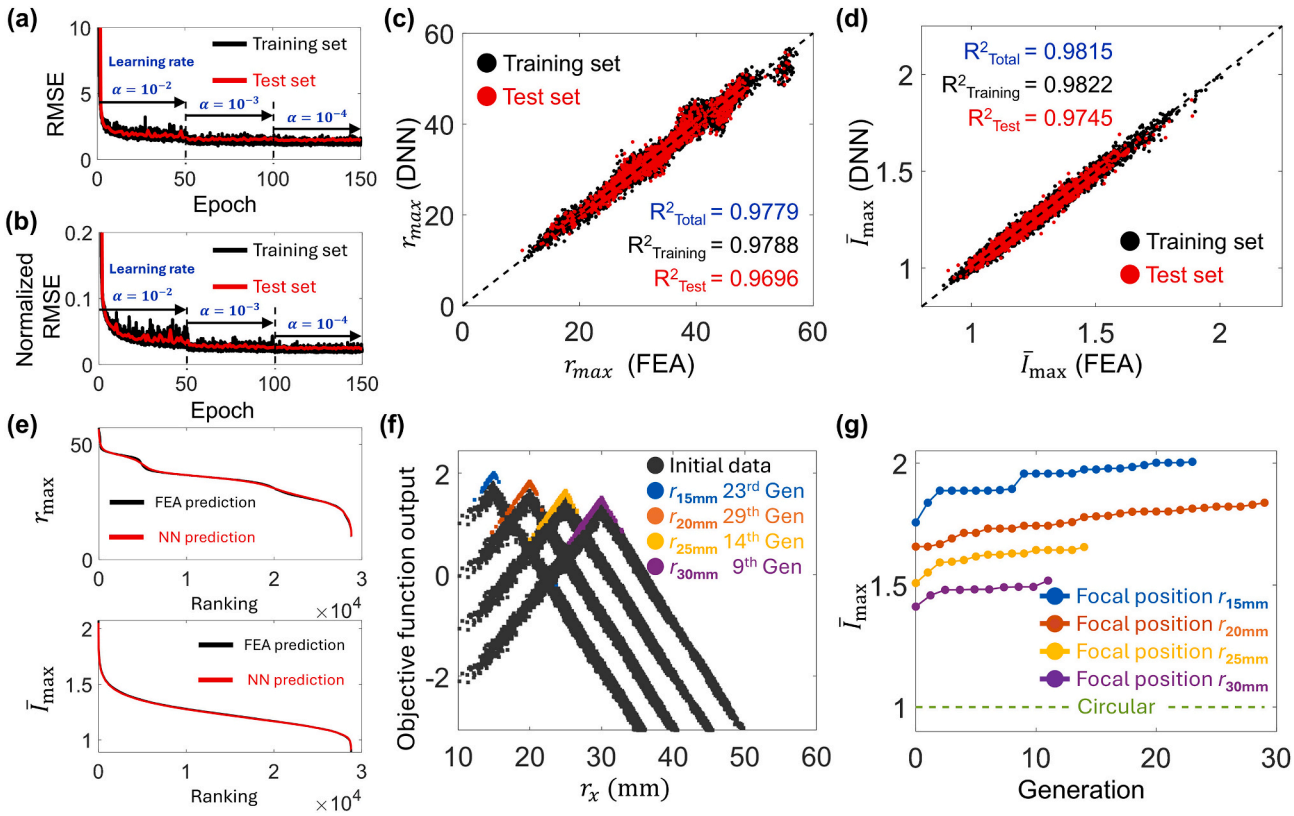


Fig. 3. DNN-based GA results. (a) Variation in RMSE with epochs number for r_{max}. (b) Variation in RMSE with epoch number for $\bar{I}_{max}$. DNN predictions and FEA results plotted against the line where the predicted values equal the actual values ($y = x$) for (c) r_{max} and (d) $\bar{I}_{max}$. (e) Predictions obtained from FEA and DNNs using the objective function ranking applied in the GA. (f) Initial dataset and objective function output in the final generation based on target focal position. (g) Variation in $\bar{I}_{max}$ with GA generation.

DNNs is examined based on permutation importance scores [55]. The importance score is defined as follows: Importance score = Permuted MSE −Original MSE. The importance score is calculated using the test datasets, with one of the 24 design variables fixed while the indices of the remaining variables are randomly shuffled. The trained DNNs predict the focal position and focused intensity, allowing for the calculation of the permuted mean-square error (MSE). An increase in the permuted MSE relative to the original MSE indicates that the corresponding design variable significantly influences the NN model's output prediction. The difference between the permuted MSE and the original MSE constitutes the importance score, which identifies key design variables influencing prediction accuracy. Figs. 4(a) and (b) show the importance scores for all the design variables of the trained model used to predict the focal position and focused intensity. The difference in the scores between the variables increases with the target focal position, and for r_{15mm}, a specific variable exhibits a significantly higher score than the other variables. Specifically, shuffling the values of X_7 yields the highest MSE for both focused intensity and focal position, which implies that X_7 is the most influential variable for the DNN's performance.

3.2. Optimization of unit-cell shape

The target focal positions are set as 15 mm, 20 mm, 25 mm, and 30 mm from the GRIN lens boundary along the symmetry line, with the objective of maximizing $\bar{I}_{max}$ to achieve optimal wave energy focusing. The iteration stops when no further improvement in $\bar{I}_{max}$ is observed. The number of generations required for convergence varies with the target focal position: 26 generations for 15 mm, 32 generations for 20 mm, 15 generations for 25 mm, and 10 generations for 30 mm. Starting from diverse initializations of the twelve Bézier control points, the GA repeatedly converged on a four-branch unit-cell shape across all target focal positions considered (Fig. S6). The optimized shape is considered the one with the best $\bar{I}_{max}$ among all the shapes that satisfy each target focal position (r_{target}). The optimized shapes for r_{15mm}, r_{20mm}, r_{25mm}, and r_{30mm} achieve their highest focused intensity within the r_{target} range in the 23rd, 29th, 14th, and 9th generations, respectively. Table S1 lists the coordinates of the control points of the Bézier curves defining the optimized unit-cell shape. Additionally, Fig. S6 demonstrates that in the generation containing the optimized shape, the top five shapes exhibit similar configurations, with a variation of less than 1 % in focal position and focused intensity. This result indicates convergence in the optimization of both shape and focused intensity.

Fig. 5(a) presents the optimized shape and FEA results for the four target focal positions. The optimized shapes demonstrate higher performance with improved $\bar{I}_{max}$ values at the target focal position compared with the circular shape. For these optimized shapes, r_{max} is 14.87, 19.86, 24.97, and 30.10 mm, aligning well with the target focal positions of 15 mm, 20 mm, 25 mm, and 30 mm, respectively; the corresponding $\bar{I}_{max}$ values are 2.00, 1.84, 1.66, and 1.52, respectively. In all cases, the optimized shape outperformed the circular shape, achieving remarkable focused intensity enhancements of 100 % at r_{15mm}, 84 % at r_{20mm}, 66 % at r_{25mm}, and 52 % at r_{30mm}. Furthermore, in the previous study, a normalized focused intensity of 1.34 was obtained at a 16.1 mm focal position [47]. However, based on the optimized results from the present study, a normalized focused intensity of 2.00 is achieved at the target focal position of 15 mm, which represents an improvement of approximately 50 % in focused intensity at a similar position.

The optimized shapes typically exhibit four branches, which are also observed in the previous work [47]. Notably, as the target position approaches the origin, the branches become thinner, leading to higher $\bar{I}_{max}$

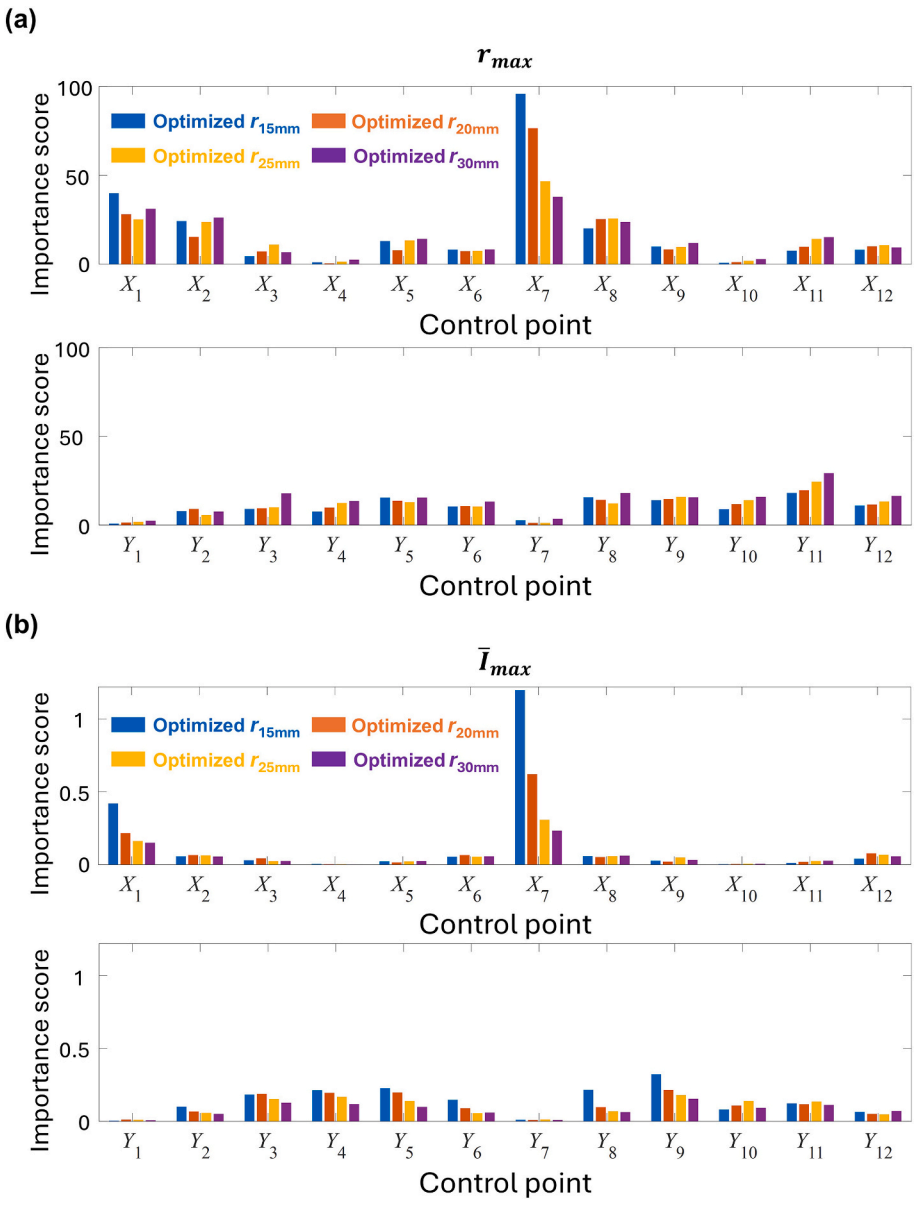


Fig. 4. Importance scores of design variables. Importance scores predicted by DNNs for (a) r_{max} and (b) $\bar{I}_{max}$.

values and a noticeable reduction in the hole area. The area of each closed shape, defined by 120,000 data points forming a closed Bézier curve, is calculated using the Shoelace formula [56]:

$$Area = \frac{1}{2}\left|\sum_{k=1}^{n-1}(x_k y_{k+1} - x_{k+1}y_k) - (x_n y_1 - x_1 y_n)\right|, (n = 120,000) \quad (3)$$

where x_k and y_k denote the coordinates of the k-th point among the 120,000 points representing the closed Bézier shape. The accuracy of the Shoelace formula is verified by calculating the area of a circular shape using the 120,000 data points, which indicates a negligible error of 4.6 $\times$ 10^{-8}. The areas of the four optimized shapes are calculated and compared with that of the shape that maximizes the focused intensity in the previous study [47]. The area of the circular shape is 12.5664 mm^2, while those of the shapes corresponding to r_{30mm}, r_{25mm}, r_{20mm}, and r_{15mm} are 7.9615 mm^2, 8.4129 mm^2, 7.7588 mm^2, and 6.8520 mm^2, respectively. The circular shape exhibits a focal position 56 mm away from the lens boundary. The optimal shape that maximized the focused intensity without any constraint on the target focal position displays an area of 6.6083 mm^2. These results indicate that the area of the optimized shape decreases as the focal position approaches the lens boundary, which corresponds to the branches becoming thinner (Fig. 5(b)).

Fig. 5(c) illustrates the normalized intensity of the optimized shape along the symmetry line. The correlation between the focal position and the focused intensity reveals that as the target focal position approaches the boundary of the GRIN lens, the focused intensity of the optimized shape increases. As the focal position moves closer to the lens, the maximum intensity increases, but the peak becomes sharper, reflecting a trade-off between energy concentration and potential distortion. Despite the absence of explicit distortion-control terms in the optimization, post-processing confirmed smooth wavefront convergence without significant side lobes. Fig. 5(d) compares the initial and optimized datasets, which include Supplementary Data at the focal positions of 10 mm, 35 mm, 40 mm, and 50 mm, as well as data optimized for the focused intensity without any constraint on the focal position. The optimal data point is used to derive a Pareto curve for $\bar{I}_{max}$ –r_{max}, which demonstrates that the focused intensity decreases with increasing target focal position. Compared with the maximum values observed in the initial dataset of 30,000 configurations, the optimized design increases the focused intensity by 14 % at r_{15mm}, 10 % at r_{20mm}, 9 % at r_{25mm}, and 7 % at r_{30mm}.

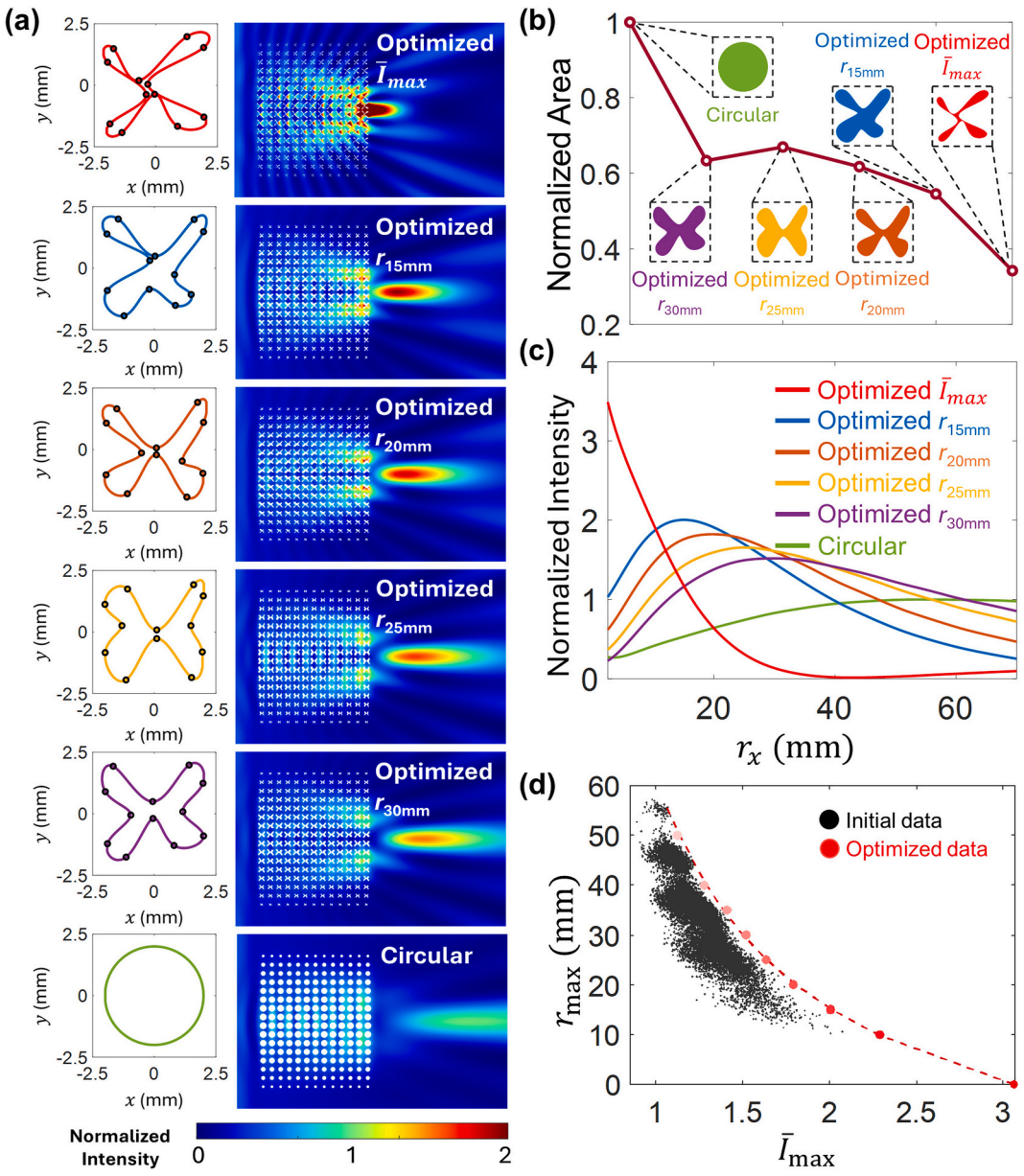


Fig. 5. Optimized shapes for target positions. (a) Optimized shape for r_{target} and corresponding FEA results. (b) Comparison between areas of optimized shapes that satisfy r_{target}. (c) Normalized intensity plot for GRIN PnCs with optimized shape. (d) Comparison between optimized and initial data highlighting the improvement in $\bar{I}_{max}$ at r_{target} for the optimized shape.

3.3. Sensitivity analysis

A sensitivity analysis is performed to evaluate the influence of the control points on the focal position and focused intensity of the optimized shape, based on the FEA results and DNN predictions. The analysis includes all 24 design variables (X_1–X_{12} and Y_1–Y_{12}) of the optimized shape (Table S1). To generate the corresponding Bézier curve, each design variable is independently perturbed by $\Delta\varepsilon = \pm 0.1$ mm while all the other variables remain fixed. This process is repeated sequentially for all design variables, resulting in 24 shapes with small variations from the original optimized shape. The focal position and focused intensity for these variations are then predicted via FEA and using the trained NN models. The central-difference method, represented by Eq. (4), is applied to calculate the sensitivity of the focal position and focused intensity for the optimized unit-cell shapes across all target positions for both the FEA and the DNN models:

$$S \approx \left| \frac{G(X_1, X_2, \cdots, X_n + \Delta\varepsilon, \cdots Y_{12}) - G(X_1, X_2, \cdots, X_n - \Delta\varepsilon, \cdots Y_{12})}{2\Delta\varepsilon} \right| \quad (4)$$

where S represents the sensitivity, which quantifies the impact of a small perturbation in the design variable on the model response, G. The response function G refers to the predicted values, such as those of the focal position and focused intensity at the focal position obtained through the FEA and using the DNNs. After introducing perturbations into the design variables, the resulting sensitivity values are examined, with high sensitivity indicating that the variable strongly impacts performance. Therefore, these variables should be considered critical during the design and manufacturing processes as they can significantly affect the performance of the final product.

Among the design variables of the optimized shapes, the ones to which the output is most sensitive are identified by normalizing the sensitivity values to a range of 0 to 1 via min–max normalization based

on the maximum and minimum output values for each shape. Fig. S7 illustrates the min–max-normalized sensitivity results mapped onto the optimized shape, providing critical insights into the influence of the design variables on the optimization outcomes. The figure includes the sensitivity analysis results obtained through the FEA and using the DNNs, showing the sensitivity of the focal position and focused intensity to changes in the design variables. The sensitivity results for the FEA and DNNs align closely, revealing consistent trends between the two methods. Table S2 presents the min–max-normalized sensitivity results for the x-coordinates and y-coordinates based on the ground-truth FEA values. Regarding the sensitivity of $\bar{I}_{max}$ to the x-coordinate across the optimized shapes for all four focal positions, the values for X_1 and X_7 are range from 0.4997 to 1.0 and 0.7232 to 1.0, respectively; thus, $\bar{I}_{max}$ demonstrates consistently high sensitivity to both these variables. In contrast, the values for X_{10} range from 0 to 0.1541, indicating low sensitivity. Based on the sensitivity analysis results for r_{max}, X_7 consistently demonstrates a strong influence on the output across the four optimized shapes, with sensitivity values ranging from 0.6429 to 1.0 (Fig. S7(a)). Regarding the y-coordinates, the sensitivity values for Y_1 range from 0 to 0.00789 while that for Y_7 remains 0, indicating low sensitivity. Fig. S7(a) further illustrates that high sensitivity is concentrated in the bottom branches and that the output exhibits low sensitivity to Y_1 and Y_7 across all optimized shapes. Similarly, Fig. S7(b) shows that the focused intensity consistently exhibits high sensitivity to X_1 and X_7 across the four optimized shapes. In contrast, among the y-coordinates, high sensitivity values ranging from 0.6635 to 1.0 are observed for Y_9, whereas Y_1 and Y_7 exhibit low sensitivity values ranging from 0 to 0.0661 and 0 to 0.0074, respectively.

Building on these findings, the physical mechanisms through which these key design variables influence the r_{max} and $\bar{I}_{max}$ are described as follows. Each control point governs a local segment of the inclusion boundary, and its perturbation directly modifies the local curvature, ligament thickness, or branch orientation, thereby altering the elastic wave propagation characteristics. In particular, Y_7 is one of the most influential variables for both r_{max} and $\bar{I}_{max}$ (Fig. S7(a) and (b)). Increasing Y_7 makes the lower branch thinner, enlarging the local solid fraction in that region, which increases the local phase velocity and steepens the refractive index gradient, thus moving the r_{max} closer to the

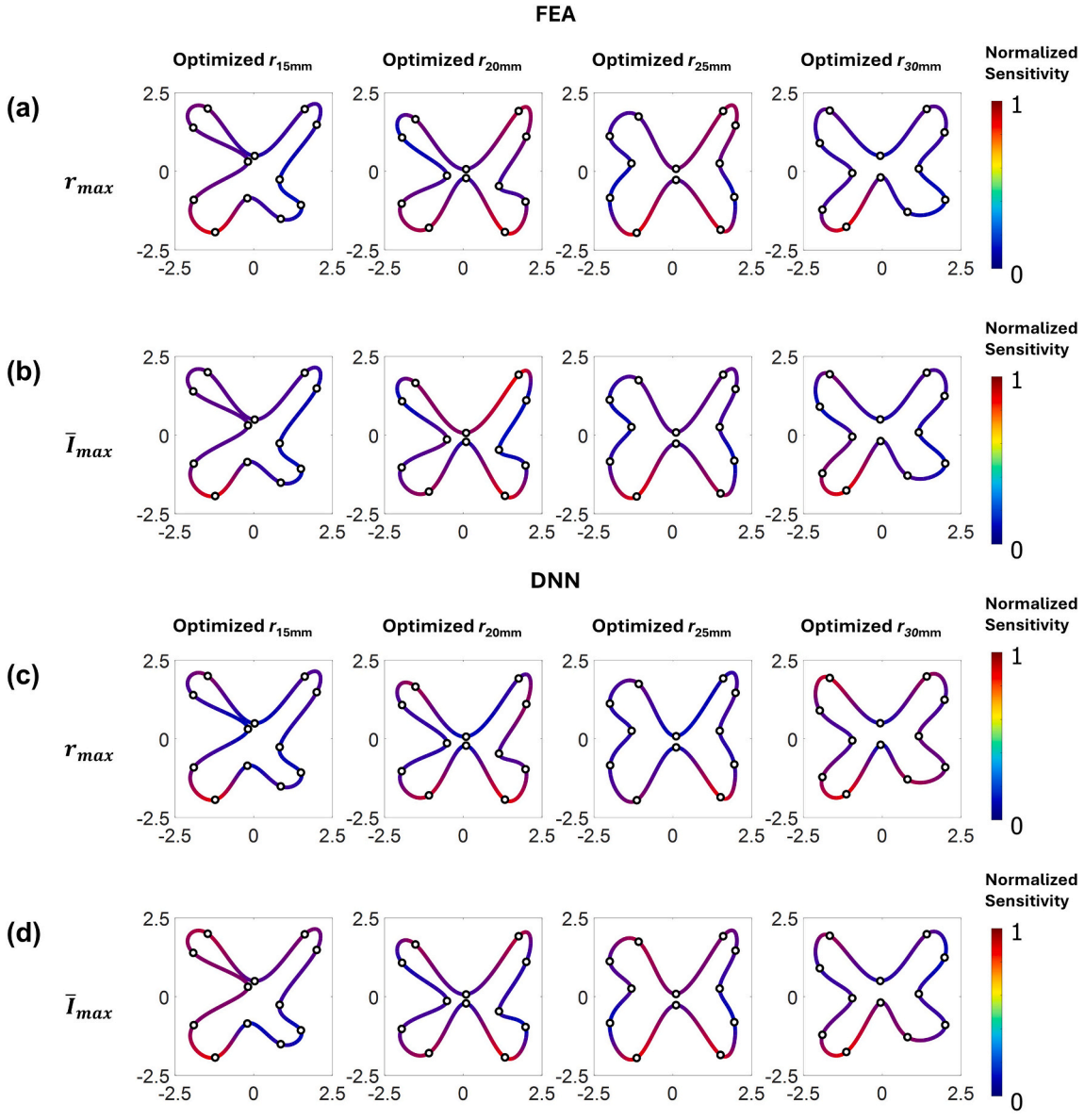


Fig. 6. Sensitivity analysis for optimized shapes. Sensitivity plots of FEA-predicted parameters for (a) r_{max} and (b) $\bar{I}_{max}$. Sensitivity plots of DNN-predicted parameters for (c) r_{max} and (d) $\bar{I}_{max}$.

lens and enhancing $\bar{I}_{max}$. Similarly, Y_9, positioned along the inner sidewall of the lower branch, shows high sensitivity to the $\bar{I}_{max}$ (Fig. S7(b)). Variations in Y_9 alter the branch's vertical alignment, influencing wave scattering toward the focal region. Unlike the key variables, coordinates such as Y_1 and Y_7 lie in regions weakly engaged by the main energy pathways and thus have negligible effect. This analysis explicitly links geometric parameters to their underlying wave-propagation mechanisms, providing a clearer physical interpretation of how local shape modifications govern the overall focusing behavior of GRIN PnCs.

Overall, X_7 consistently exhibits a strong impact on both focal position and focused intensity; hence, it is the most critical design variable for the performance of GRIN PnCs. This inference is corroborated by the high importance score of X_7 (Figs. 4(a) and (b)). Conversely, Y_1 and Y_7, which have low sensitivity values, also display low importance scores; this indicates a strong correlation between the sensitivity results and the importance scores. Therefore, X_7 represents a key design variable, whereas Y_1 and Y_7 are deemed less important.

The average sensitivity of the output to each control point—combining the sensitivities to both the x-coordinate and y-coordinate—is calculated using the following equation:

$$S_{avg} = \frac{S_{X_n} + S_{Y_n}}{2} (n : control\ point\ index) \quad (5)$$

where S_{Xn} and S_{Yn} represent the sensitivities to the x-coordinate and y-coordinate of the control point, respectively. Fig. 6 depicts the optimized shape corresponding to the min–max-normalized average sensitivity (S_{avg}). Figs. 6(a) and (c) present the sensitivity analysis results for the focal position, while Figs. 6(b) and (d) present the results for the focused intensity. The agreement between the FEA and DNN results highlights the remarkable prediction accuracy of the DNNs for gradient calculation.

A sensitivity analysis is also conducted based on the control points used in the experiments from the previous study to explain the discrepancies between the experimental and simulation results [47]. Fig. 7(a) shows that regions with high sensitivity are concentrated in the branches of the shape, with particularly high $\bar{I}_{max}$ values observed at P_3

Table 2
Min–max-normalized sensitivity of focused intensity to experimental control points from the previous study [47].

Control point	Normalized S_{avg}
P_1	0.6294
P_2	0.5071
P_3	0.9974
P_4	0.4088
P_5	0.0301
P_6	0.1008
P_7	0
P_8	0.3338
P_9	1
P_{10}	0.0760
P_{11}	0.7259
P_{12}	0.6968

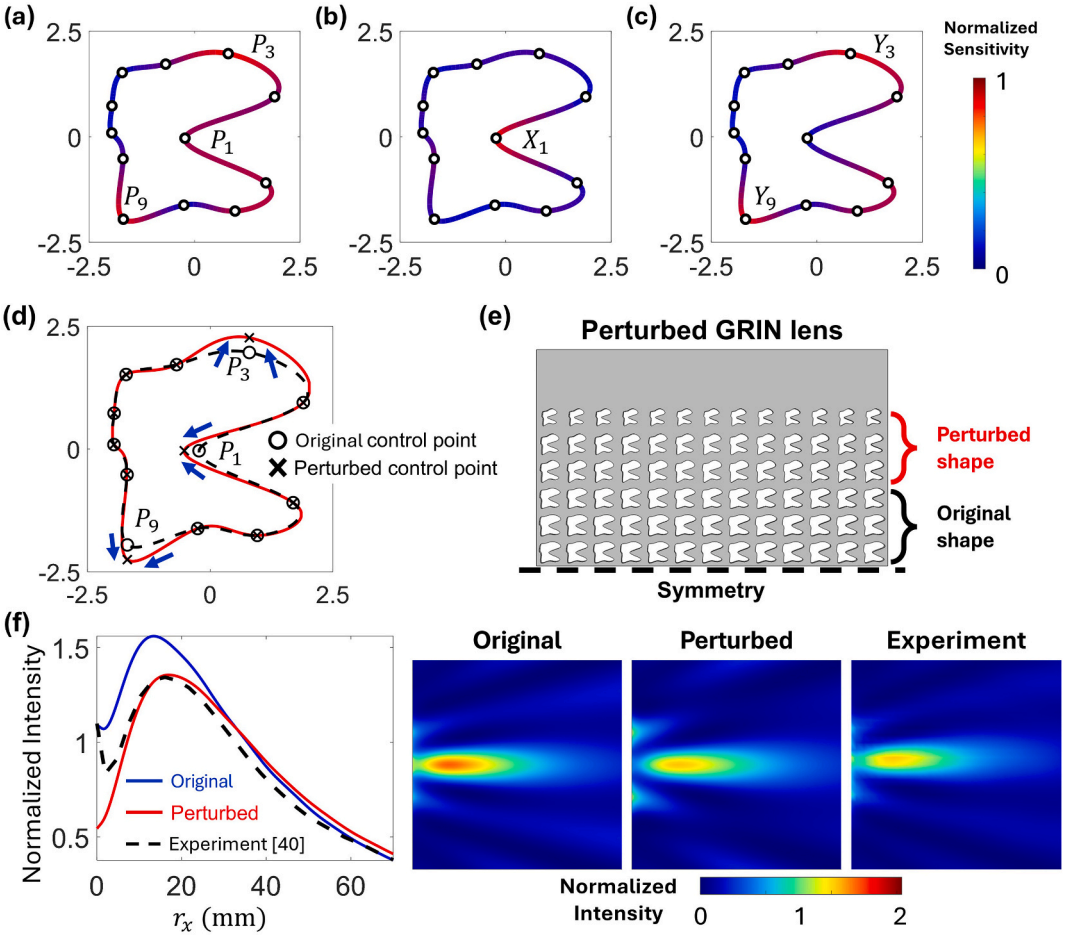


Fig. 7. Validation of sensitivity analysis conducted on experimental shape. (a) Normalized S_{avg} results. Sensitivity of focused intensity to perturbations in (b) x-coordinates and (c) y-coordinates. (d) Perturbed shape obtained by shifting control points P_1, P_3, and P_9. (e) Perturbed GRIN lens with the perturbed shapes in the top three layers. (f) Comparison of normalized intensity plots and FEA results among GRIN PnCs with the original shape, the perturbed shape, and experimental data from the previous study [47].

(0.99) and P_9 (1.0), (Table 2). To investigate these findings further, the sensitivity to the x-coordinates and y-coordinates is analyzed in detail. Figs. 7(b) and (c) indicate that the focused intensity is highly sensitive to X_1, Y_3, and Y_9. Minor perturbations are applied to the control points with high sensitivity values, and Fig. 7(d) shows the resulting perturbed shape. Based on the experimental findings from the previous study, a GRIN lens with 12 layers was fabricated, considering the constrained imposed by the manufacturing resolution limit [47]. The top three layers, with scaling factors of 0.7–0.9, are particularly challenging to fabricate due to their smaller size. A perturbed GRIN lens with the perturbed shape is also designed and is applied to the top three layers of the original GRIN lens (Fig. 7(e)). Fig. 7(f) compares the FEA results with the experimental findings from the previous study. GRIN PnCs fabricated based on the original shape exhibited a focal position at 13.4 mm along with a normalized focused intensity of 1.56, whereas GRIN PnCs prepared with the perturbed design displayed a shift in the focal position to 16.9 mm and a normalized focused intensity of 1.35. The experimentally measured focal position and normalized focused intensity were 16.1 mm and 1.34, respectively. Thus, the properties of the perturbed GRIN PnCs closely align with the experimental results, showing only a 4.9 % deviation in the focal position and a 0.7 % error in the normalized focused intensity. The agreement between the experimental findings and the sensitivity analysis results, which identify the sensitive control points, provides reliable insights. The performance parameters of the optimized shapes exhibit heightened sensitivity to control points in the branches, which emphasizes the importance of precise branch fabrication for setting the focal position accurately and maximizing the focused intensity.

The proposed DNN-based GA efficiently explores a high-dimensional design space, achieving enhanced focusing intensity and tunable focal positions within realistic manufacturing constraints. Although this study primarily addresses theoretical optimization and simulation, physical verification is essential to confirm performance under practical conditions. In our previous work [47], a GRIN PnC lens fabricated within CNC machining tolerances showed good agreement between measured and simulated results, demonstrating practical feasibility. Building on this foundation, the present designs incorporate tunable focal positions and a sensitivity analysis to identify geometry parameters—particularly control points in the lower branch region—most critical to robust performance. For practical CNC implementation, one feasible experimental scheme is to configure all layers so they can be machined with a 1 mm radius end mill, ensuring compatibility with standard CNC machining processes. Sensitivity validation could then be conducted by deliberately introducing manufacturing tolerances into the high-sensitivity regions identified in this study and measuring the resulting variations in focal position and intensity. This strategy would enable a realistic and direct assessment of the robustness and applicability of the proposed GRIN PnC designs under real-world fabrication constraints.

4. Conclusion

In this study, a DNN-accelerated GA is used to optimize the unit-cell shape of GRIN PnCs for enhanced energy focusing. DNNs are employed to model the complex relationship between the control points of the shape, the focal position, and the focused intensity. The trained model predicts significant control points. The unit cells are optimized for various target focal positions, with the results revealing a trade-off between the focal position and the focused intensity as well as highlighting a limit to the maximum focused intensity achievable for distant focal positions. Compared with the conventional circular model, the optimized designs exhibit a 1.5 to 2.0 times higher focused intensity across the target focal positions. The optimized shapes, characterized by four branches, exhibit high sensitivity to some of the design parameters, which underscores the importance of precise fabrication. The sensitivity analysis further facilitates the identification of critical design variables, enabling a more efficient and robust fabrication process. These findings contribute to the advancement of EH by providing a systematic approach to designing high-performance GRIN PnCs. However, this study primarily focused on energy concentration along the centerline of GRIN PnCs. To develop efficient EH systems that can adapt to varying operating conditions, future studies should consider regions beyond the centerline as well. Efforts to this end will be essential for enhancing the adaptability and overall effectiveness of EH systems.

CRediT authorship contribution statement

Mary Kim: Writing – review & editing, Writing – original draft, Validation, Methodology, Investigation, Formal analysis, Data curation. **Sangryun Lee:** Writing – review & editing, Writing – original draft, Supervision, Project administration, Funding acquisition, Conceptualization.

Funding

This work was supported by the National Research Foundation of Korea(NRF) grant funded by the Korea government(MSIT) (RS-2025-24803153).

Declaration of competing interest

The authors declare that they have no known competing financial interests or personal relationships that could have appeared to influence the work reported in this paper.

Appendix A. Supplementary data

Supplementary data to this article can be found online at https://doi.org/10.1016/j.matdes.2025.114723.

Data availability

Data will be made available on request.

References

[1] Y. Du, et al., Energy transfer and redistribution: an approach for unifying vibrational energy harvesting and vibration attenuation, Nano Energy 78 (2020) 105245, https://doi.org/10.1016/j.nanoen.2020.105245.
[2] D.N. Hao, et al., Solar energy harvesting technologies for PV self-powered applications: a comprehensive review, Renew. Energy 188 (2022) 678–697, https://doi.org/10.1016/j.renene.2022.02.066.
[3] C. Zhang, et al., High space efficiency hybrid nanogenerators for effective water wave energy harvesting, Adv. Funct. Mater. 32 (18) (2022) 2111775, https://doi.org/10.1002/adfm.202111775.
[4] X. Zhao, et al., A soft magnetoelastic generator for wind-energy harvesting, Adv. Mater. 34 (38) (2022) e2204238, https://doi.org/10.1002/adma.202204238.
[5] R.Y. Yu, et al., Ambient energy harvesters in wearable electronics: fundamentals, methodologies, and applications, J. Nanobiotechnol. 22 (1) (2024), https://doi.org/10.1186/s12951-024-02774-0.
[6] Z.Q. Lu, et al., Ocean wave energy harvesting with high energy density and self-powered monitoring system, Nat. Commun. 15 (1) (2024) 6513, https://doi.org/10.1038/s41467-024-50926-5.
[7] S. Panda, et al., Piezoelectric energy harvesting systems for biomedical applications, Nano Energy 100 (2022) 107514, https://doi.org/10.1016/j.nanoen.2022.107514.
[8] Y. Zou, V. Raveendran, J. Chen, Wearable triboelectric nanogenerators for biomechanical energy harvesting, Nano Energy 77 (2020), https://doi.org/10.1016/j.nanoen.2020.105303.
[9] W. Xian, S. Lee, A pendulum based frequency-up conversion mechanism for vibrational energy harvesting in low-speed rotary structures, J. Intell. Mater. Syst. Struct. 35 (12) (2024) 1040–1056, https://doi.org/10.1177/1045389X241232044.
[10] K.X. Huang, et al., The optimal design of a piezoelectric energy harvester for smart pavements, Int. J. Mech. Sci. 232 (2022), https://doi.org/10.1016/j.ijmecsci.2022.107609.
[11] W. Hwang, et al., Watts-level road-compatible piezoelectric energy harvester for a self-powered temperature monitoring system on an actual roadway, Appl. Energy 243 (2019) 313–320, https://doi.org/10.1016/j.apenergy.2019.03.122.

[12] J.Y. Cho, et al., Design of optimized cantilever form of a piezoelectric energy harvesting system for a wireless remote switch, Sens. Actuat. A-Phys. 280 (2018) 340–349, https://doi.org/10.1016/j.sna.2018.07.023.
[13] M. Shirvanimoghaddam, et al., Towards a green and self-powered internet of things using piezoelectric energy harvesting, IEEE Access 7 (2019) 94533–94556, https://doi.org/10.1109/ACCESS.2019.2928523.
[14] J.H. Kim, et al., Development of a hybrid type smart pen piezoelectric energy harvester for an IoT platform, Energy 222 (2021), https://doi.org/10.1016/j.energy.2021.119845.
[15] M.H. Lu, L. Feng, Y.F. Chen, Phononic crystals and acoustic metamaterials, Mater. Today 12 (12) (2009) 34–42, https://doi.org/10.1016/S1369-7021(09)70315-3.
[16] X. Zhang, Z. Liu, Negative refraction of acoustic waves in two-dimensional phononic crystals, Appl. Phys. Lett. 85 (2) (2004) 341–343, https://doi.org/10.1063/1.1772854.
[17] W. Kuang, Z. Hou, Y. Liu, The effects of shapes and symmetries of scatterers on the phononic band gap in 2D phononic crystals, Phys. Lett. A 332 (5–6) (2004) 481–490, https://doi.org/10.1016/j.physleta.2004.10.009.
[18] M.S. Kushwaha, et al., Theory of acoustic band structure of periodic elastic composites, Phys. Rev. B Condens. Matter 49 (4) (1994) 2313–2322, https://doi.org/10.1103/PhysRevB.49.2313.
[19] E. Panahi, et al., Novel cross shape phononic crystals with broadband vibration wave attenuation characteristic: design, modeling and testing, Thin-Walled Struct. 163 (2021), https://doi.org/10.1016/j.tws.2021.107665.
[20] J.O. Vasseur, et al., Experimental and theoretical evidence for the existence of absolute acoustic band gaps in two-dimensional solid phononic crystals, Phys. Rev. Lett. 86 (14) (2001) 3012–3015, https://doi.org/10.1103/PhysRevLett.86.3012.
[21] Y. Bao, et al., Phononic crystal-based acoustic demultiplexer design via bandgap-passband topology optimization, Composite Struct. (2025) 351, https://doi.org/10.1016/j.compstruct.2024.118622.
[22] Z.Y. Jia, et al., Maximizing acoustic band gap in phononic crystals via topology optimization, Int. J. Mech. Sci. (2024) 270, https://doi.org/10.1016/j.ijmecsci.2024.109107. ARTN 109107.
[23] D.H. Han, et al., Study on bandgap of a novel phononic crystal with low-frequency sound insulation, AIP Adv. 12 (5) (2022), https://doi.org/10.1063/5.0085368.
[24] L.J. Li, et al., Design of phononic crystals plate and application in vehicle sound insulation, Adv. Eng. Softw. 125 (2018) 19–26, https://doi.org/10.1016/j.advengsoft.2018.08.002.
[25] Y.-J. Liang, et al., An acoustic absorber implemented by graded index phononic crystals, J. Appl. Phys. 115 (24) (2014), https://doi.org/10.1063/1.4885459.
[26] Y.F. Wang, et al., Channeled spectrum in the transmission of phononic crystal waveguides, J. Sound Vib. 437 (2018) 410–421, https://doi.org/10.1016/j.jsv.2018.09.030.
[27] A. Khelif, et al., Guiding and bending of acoustic waves in highly confined phononic crystal waveguides, Appl. Phys. Lett. 84 (22) (2004) 4400–4402, https://doi.org/10.1063/1.1757642.
[28] Z.H. Jiang, et al., Waveguides induced by replacing defects in phononic crystal, Int. J. Mech. Sci. 255 (2023), https://doi.org/10.1016/j.ijmecsci.2023.108464.
[29] H.B. Huang, et al., Topologically protected zero refraction of elastic waves in pseudospin-Hall phononic crystals, Commun. Phys. 3 (1) (2020) 46, https://doi.org/10.1038/s42005-020-0314-6.
[30] H.B. Huang, S.Y. Huo, J.J. Chen, Subwavelength elastic topological negative refraction in ternary locally resonant phononic crystals, Int. J. Mech. Sci. 198 (2021) 106391, https://doi.org/10.1016/j.ijmecsci.2021.106391.
[31] J.J. Chen, et al., Self-ordering induces multiple topological transitions for in-plane bulk waves in solid phononic crystals, Phys. Rev. B. 98 (1) (2018) 014302, https://doi.org/10.1103/PhysRevB.98.014302.
[32] C.S. Park, et al., Two-dimensional octagonal phononic crystals for highly dense piezoelectric energy harvesting, Nano Energy 57 (2019) 327–337, https://doi.org/10.1016/j.nanoen.2018.12.026.
[33] H.Y. Lv, et al., Vibration energy harvesting using a phononic crystal with point defect states, Appl. Phys. Lett. 102 (3) (2013), https://doi.org/10.1063/1.4788810.
[34] G.Y. Zhang, et al., Phononic crystals with incomplete line defects: applications in high-performance and broadband acoustic energy localization and harvesting, Smart Mater. Struct. 33 (8) (2024), https://doi.org/10.1088/1361-665X/ad649c.
[35] F.Y. Ma, et al., Acoustic focusing and imaging via phononic crystal and acoustic metamaterials, J. Appl. Phys. 131 (1) (2022), https://doi.org/10.1063/5.0074503.
[36] K. Yi, et al., Enhancement of elastic wave energy harvesting using adaptive piezo-lens, Mech. Syst. Sig. Process. 93 (2017) 255–266, https://doi.org/10.1016/j.ymssp.2017.02.008.
[37] S. Tol, F.L. Degertekin, A. Erturk, 3D-printed phononic crystal lens for elastic wave focusing and energy harvesting, Addit. Manuf. 29 (2019), https://doi.org/10.1016/j.addma.2019.100780.
[38] F. Ahmadzadeh, A. Bahrami, Mechanically tuned gradient-index phononic crystal lens, Chin. J. Phys. 77 (2022) 2773–2780, https://doi.org/10.1016/j.cjph.2022.05.012.
[39] S.-C.-S. Lin, et al., Gradient-index phononic crystals, Phys. Rev. B 79 (2009) 9, https://doi.org/10.1103/PhysRevB.79.094302.
[40] S. Tol, F.L. Degertekin, A. Erturk, Phononic crystal Luneburg lens for omnidirectional elastic wave focusing and energy harvesting, Appl. Phys. Lett. 111 (1) (2017), https://doi.org/10.1063/1.4991684.
[41] N. Shen, et al., Design of phononic crystals using superposition of defect and gradient-index for enhanced wave focusing, Smart Mater. Struct. 33 (8) (2024), https://doi.org/10.1088/1361-665X/ad62cb.
[42] H. Danawe, S. Tol, Conformal gradient-index phononic crystal lenses: Design, theory, and application on non-planar structures, Mater. Design 253 (2025) 113854, https://doi.org/10.1016/j.matdes.2025.113854.
[43] J. Hyun, W. Choi, M. Kim, Gradient-index phononic crystals for highly dense flexural energy harvesting, Appl. Phys. Lett. 115 (17) (2019), https://doi.org/10.1063/1.5111566.
[44] S.C. Lin, B.R. Tittmann, T.J. Huang, *Design of acoustic beam aperture modifier using gradient-index phononic crystals*, J. Appl. Phys. 111 (12) (2012) 123510, https://doi.org/10.1063/1.4729803.
[45] W.M. Lee, *Acoustic scattering by multiple elliptical cylinders using collocation multipole method*, J. Comput. Phys. 231 (14) (2012) 4597–4612, https://doi.org/10.1016/j.jcp.2012.02.032.
[46] S. Acosta, *On-surface radiation condition for multiple scattering of waves*, Comput. Methods Appl. Mech. Eng. 283 (2015) 1296–1309, https://doi.org/10.1016/j.cma.2014.08.022.
[47] S. Lee, et al., Machine learning-enabled development of high performance gradient-index phononic crystals for energy focusing and harvesting, Nano Energy 103 (2022) 107846, https://doi.org/10.1016/j.nanoen.2022.107846.
[48] S.H. Han, Q. Han, C.L. Li, Deep-learning-based inverse design of phononic crystals for anticipated wave attenuation, J. Appl. Phys. 132 (15) (2022), https://doi.org/10.1063/5.0111182.
[49] X. Li, et al., Designing phononic crystal with anticipated band gap through a deep learning based data-driven method, Comput. Methods Appl. Mech. Eng. 361 (2020), https://doi.org/10.1016/j.cma.2019.112737.
[50] P. Kudela, et al., Deep learning aided topology optimization of phononic crystals, Mech. Syst. Sig. Process. 200 (2023), https://doi.org/10.1016/j.ymssp.2023.110636.
[51] M. Rupin, et al., *Experimental demonstration of ordered and disordered multiresonant metamaterials for lamb waves*, Phys. Rev. Lett. 112 (23) (2014) 234301, https://doi.org/10.1103/PhysRevLett.112.234301.
[52] S. COMSOL Multiphysics®. www.comsol.com. COMSOL AB, Sweden.
[53] K. He, et al., Deep residual learning for image recognition, in: Proceedings of the IEEE Conference on Computer Vision and Pattern Recognition, 2016, https://doi.org/10.1109/CVPR.2016.90.
[54] S. Lee, Z. Zhang, G.X. Gu, Generative machine learning algorithm for lattice structures with superior mechanical properties, Mater. Horiz. 9 (3) (2022) 952–960, https://doi.org/10.1039/D1MH01792F.
[55] S.S. Xie, L.L. Gu, J.P. Guo, Design of chiral plasmonic metamaterials based on interpretable deep learning, J. Phys. D-Appl. Phys. 57 (4) (2024), https://doi.org/10.1088/1361-6463/ad0567.
[56] K.M. Dogan, H. Suzuki, Sample management system based on functionality through user-defined geometric constraints, Comput.-Aided Des. Appl. (2023), https://doi.org/10.14733/cadaps.2023.190-212.